

Coupling phase field and visco-plasticity to study rafting in Ni-base superalloys

Anaïs Gaubert, Yann Le Bouar, Alphonse Finel

▶ **To cite this version:**

Anaïs Gaubert, Yann Le Bouar, Alphonse Finel. Coupling phase field and visco-plasticity to study rafting in Ni-base superalloys. Philosophical Magazine, 2010, 90 (01-04), pp.375-404. 10.1080/14786430902877802 . hal-00556061

HAL Id: hal-00556061
https://hal.science/hal-00556061

Submitted on 15 Jan 2011

HAL is a multi-disciplinary open access archive for the deposit and dissemination of scientific research documents, whether they are published or not. The documents may come from teaching and research institutions in France or abroad, or from public or private research centers.

L'archive ouverte pluridisciplinaire **HAL**, est destinée au dépôt et à la diffusion de documents scientifiques de niveau recherche, publiés ou non, émanant des établissements d'enseignement et de recherche français ou étrangers, des laboratoires publics ou privés.



Coupling phase field and visco-plasticity to study rafting in Ni-base superalloys

Journal:	*Philosophical Magazine & Philosophical Magazine Letters*
Manuscript ID:	TPHM-09-Jan-0032
Journal Selection:	Philosophical Magazine
Date Submitted by the Author:	21-Jan-2009
Complete List of Authors:	Gaubert, Anaïs; Onera, DMSM/CEMN Le Bouar, Yann; Onera/CNRS, Laboratoire d'Etude des Microstructures Finel, Alphonse; Onera/CNRS, Laboratoire d'Etude des Microstructures
Keywords:	microstructure change, Ni-based superalloys, plasticity
Keywords (user supplied):	phase field, rafting
Note: The following files were submitted by the author for peer review, but cannot be converted to PDF. You must view these files (e.g. movies) online.	
article.tex	

scholarONE™
Manuscript Central

Philosophical Magazine
Vol. 00, No. 00, 21 December 2008, 1–26

RESEARCH ARTICLE

Coupling phase field and visco-plasticity to study rafting in Ni-base superalloys

A. Gaubert[a*], Y. Le Bouar[b] and A. Finel[b]

[a]*Onera, 29 avenue de la Division Leclerc, 92320 Châtillon, France*; [b]*Laboratoire d'Etude des Microstructures, Onera/CNRS, 29 avenue de la Division Leclerc, 92320 Châtillon, France*,

(*January 21, 2009*)

An elasto-visco-plastic model is developed to study the microstructural evolution during a creep loading in a model AM1 superalloy. Elastic anisotropy and inhomogeneity, as well as the description of long range order in the γ' phase are included in the model. Plastic activity is introduced using a continuum crystal plasticity framework at mesoscale. A special attention is paid on the corresponding parameters identification from experiments. Two dimensional simulations of creep in the [100] direction are performed, and the results are compared to the predictions of an elastic phase field model, in order to characterize the influence of plastic activity on the microstructural evolution. In particular, our simulations show that plastic activity in the γ channels significantly increases the rafting kinetics and allows misalignments of rafts with respect to cubic directions. The simulation results are critically discussed and improvements of the model are proposed.

Keywords: Nickel-base superalloys, rafting, phase field, visco-plasticity

1. Introduction

Nickel-base superalloys are widely used in aero-engine industries for turbine blades designing because of their outstanding mechanical behavior at high temperatures. They owe these properties to their typical microstructure consisting of cuboids of γ' precipitates surrounded by thin channels of γ matrix. Indeed, the γ' phase is ordered (in a $L1_2$ Ni_3Al type structure) and its dispersion in the γ (face-centered cubic nickel-rich disordered phase) matrix reduces dislocations motion. However, when loaded at high temperature, the microstructure undergo the so-called rafting phenomenon. During a $\langle 001 \rangle$ oriented creep test, the precipitates coarsen in an anisotropic way to form platelets [1–4].

A great number of models has been developed in order to predict rafts orientation, first in an elastic framework [5] and more recently adding the plastic strains influence [6–9]. These models have pointed out driving forces on rafting such as the lattice misfit, the external loading and its direction with respect to the microstructure orientation and the difference in elastic constants between the two phases. In the mean time, the plastic activity in γ channels is also pointed out as an important parameter on directional coalescence of γ' precipitates. This point has been illustrated experimentally in [10] where the AM1 superalloy is loaded at a temperature too low to observe rafting and then submitted to a higher temperature

*Corresponding author. Email: anais.gaubert@onera.fr

ISSN: 1478-6435 print/ISSN 1478-6443 online
© 2008 Taylor & Francis
DOI: 10.1080/1478643YYxxxxxxxx
http://www.informaworld.com

For Peer Review Only

without applied stress. This test shows that rafting occurs at high temperature due to the dislocations created at the lower temperature. Other authors [11, 12] have carried out similar experiments showing that without plasticity rafting is too slow to be observed. Dislocations partially relax coherency stresses in the horizontal matrix channels and increase them in others, so that it affects the driving forces on diffusion [13]. They also provide fast diffusion paths [14].

As it has been said, several models have been developed in order to predict basic features of the coarsened microstructure such as the raft orientation dependence on driving forces. However, the prediction of the rafting kinetics and of the microstructural evolution (e.g. shape and size of the rafts) is more difficult. The phase field method, which is appropriate to reproduce microstructural evolution on large length and time scales, is particularly suited to tackle this problem. The phase field method has been thoroughly used to study microstructural evolution inherited from solid-solid phase transformations when elastic stresses are generated in the microstructure (e.g. [15–17]). The microstructural evolution under applied load has also been studied using phase field models by several authors [18, 19]. However, a phase field model developed for studying rafting in superalloys should include, not only the driving forces originating from the elastic fields, but also the driving forces resulting from the plastic strain fields. What we propose here is to develop such a phase field model by explicitly introducing the plastic strains fields in the model.

In one hand, plastic activity in phase field has already been treated by modeling the dislocations [20, 21] and their dynamics [22–25]. Dislocations are represented by their plastic eigenstrains and act individually through the elastic field they generate. Large scale simulations taking into account the mutual interaction between all the glide systems and the evolving γ/γ' microstructure is computationally very intensive. Indeed, in this phase field approach of plasticity, the dislocation core size is equal to several times the grid spacing. Consequently, the description of a realistic dislocation core size, which is important for the short range interaction between dislocations, requires a subnanometer grid size. This limit in the simulation grid size does not allow simulations at the micron scale. However this method has been recently used to show that plasticity plays a dominant role in the rafting process compared to elastic misfit [25].

On the other hand, plastic activity can also be added to the phase field model by introducing a plastic strain field defined at mesoscale. A crude version of this approach was proposed in [26] where a decrease in the lattice misfit accounts for the consequences of plastic activity. A precipitates disorientation for long creep time, as it can be seen in experiments, has been obtained [26]. Another version of this approach has been recently proposed in [9] where the plastic strain is related to the inter dislocations distance, the later beeing assumed equal in all matrix channels of the microstructure.

The present contribution aims at developing a more physical method, but not too intensive in order to be able to simulate realistic systems. The phenomenological visco-plasticity framework seems to be a good solution as it has been shown in a recent study of Ni base superalloys under creep loading [27]. Few other attempts have been proposed in that way, but applied to different alloys. [28] have studied mechanical behavior of tin-lead solder during the evolution of the microstructure. However, in this paper, the influence of plasticity on the microstructure evolution is not taken into account. More complete coupling has been proposed very recently [29, 30], respectively for grain growth and hydride precipitation in zirconium.

As explained above, the aim of the present paper is to study the microstructural evolution in the AM1 superalloy during creep. The paper is organized as follows.

For Peer Review Only

In section 2, we detail the phase field model that we have used to predict the microstructural evolution when plastic activity can be neglected. We show the ability of this model, which takes into account elastic inhomogeneity, to predict the microstructure evolution in the AM1 superalloy during an annealing at 950°C. In section 3, the framework of phenomenological visco-plasticity is presented and we show how to determine visco-plastic parameters which are relevant for the γ and γ' phases in the AM1 superalloy. In section 4 we develop a new model able to describe the microstructure evolution in the presence of plastic activity. This is achieved by coupling the phase field model with the visco-plastic equations. In section 5, the microstructural evolution during creep is considered and our model is used to illustrate the influence of plastic activity. In the last section, the simulation results are critically discussed and improvements of the model are proposed.

In this work, $\underline{\mathbf{a}}$ denotes a vector of the Euclidean space, $\underset{\sim}{\mathbf{A}}$ a second-rank Euclidean tensor and $\underset{\approx}{\mathbf{A}}$ a fourth-rank Euclidean tensor.

2. The phase field model

The phase field model developed in this section is devoted to the microstructural evolution in Ni-base superalloys. The model is based on a description of the microstructure at mesoscale by a set of concentration and long range order fields.

The first field is the concentration field $c(\underline{\mathbf{r}}, t)$, defined as the local Al atomic concentration. Other concentration fields are in principle necessary to fully describe a multicomponent superalloy such as the AM1 [31]. However, assuming that the minority elements added to Ni and Al, do not qualitatively modify the physical mechanisms responsible for the microstructural evolution, the multicomponent superalloy can be modeled as an effective binary superalloy. In that case, the only difference between a binary and a multicomponent superalloy is the values of the physical parameters used for the calibration of the model, such as the diffusion coefficient, the onset of plastic activity, the viscosity parameters, etc..

In the case of the $\gamma \rightarrow \gamma'$ phase ordering involved in the precipitation process, three order parameter fields have to be introduced to account for the degeneracy of the low temperature γ' phase. These order parameters, related to symmetry reduction of the ordering process, are classically defined using the concentration wave formalism [32]. The four translational variants of the γ' phase (with the stoechiometry Ni_3Al) are then obtained for the following long-range order parameters: $\{\eta_1, \eta_2, \eta_3\} = \eta_0\{1,1,1\}$, $\eta_0\{\bar{1},\bar{1},1\}$, $\eta_0\{\bar{1},1,\bar{1}\}$, $\eta_0\{1,\bar{1},\bar{1}\}$. Note that the degeneracy of the γ' phase plays an important role in the coarsening regime of AM1 alloys where the volume fraction is very high (about 68% [33])

The main ingredient of the phase field modeling is a mesoscopic free energy functional F that makes a link between a microstructure, i.e. the concentration and order parameter fields, and and its total free energy. The free energy functional F accounts for the bulk free energy, the surface energies as well as for the elastic energy. These contributions are detailed in the next subsections. The evolution of each field is obtained by solving a kinetic equation that is governed by a corresponding driving force, related to the functional derivative of the total free energy with respect to the field. Assuming that the field evolution is linear with respect to the driving force, we obtain the Cahn-Hilliard equation for the concentration field, which is a conserved field, and the Allen-Cahn equation for the order parameter

For Peer Review Only

fields which are not conserved

$$\frac{\partial c}{\partial t} = M\nabla^2 \frac{\delta F}{\delta c} \tag{1}$$

$$\frac{\partial \eta_i}{\partial t} = -L\frac{\delta F}{\delta \eta_i} \tag{2}$$

where the kinetic coefficient L and the mobility coefficient M are assumed constant. Gaussian distributed noise terms are classically added to the right hand side of 1 and 2 to reproduce thermal fluctuations (e.g. [16]). The correlation properties of the noise terms are usually selected to meet the requirements of the fluctuation-dissipation theorem which ensures that the equilibrium fluctuations are correctly reproduced. Note however that it does not imply that the model is relevant to quantitatively describe the first stages of the precipitation process, especially when the precipitation starts by a nucleation mechanism [34].

2.1. *The Ginzburg-Landau free energy*

This subsection details the choice of the chemical part of the free energy F_{GL} which is suited for a $\gamma + \gamma'$ mixture.

2.1.1. Free energy density of an homogeneous microstructure

The free energy density $f_{homo}(c, \{\eta_i\})$ of an homogeneous system characterized by the concentration c and the order parameters η_i should be invariant with respect to the symmetry operation of the high temperature structure. As usual, we approximate $f_{homo}(c, \{\eta_i\})$ using a polynomial expansion with respect to the order parameters. Following [26], we stop the polynomial expansion to the lowest possible order and we assume a very simple concentration dependance for the coefficients of the expansion

$$f_{homo}(c, \{\eta_i\}) = \Delta f \left[\frac{1}{2}(c - c_\gamma)^2 + \frac{\mathcal{B}}{6}(c_2 - c) \sum_{i=1,3} \eta_i^2 - \frac{\mathcal{C}}{3}\eta_1\eta_2\eta_3 + \frac{\mathcal{D}}{12} \sum_{i=1,3} \eta_i^4 \right] \tag{3}$$

Δf is the energy density scale of the model and c_2 is an arbitrary concentration chosen between the equilibrium concentrations c_γ and $c_{\gamma'}$ of the coexisting phases. $\mathcal{B}$, $\mathcal{C}$ and $\mathcal{D}$ are constants related to c_2, c_γ, $c_{\gamma'}$ and to the equilibrium long-range order parameter η_0 through

$$\begin{aligned} \mathcal{B} &= \frac{2}{\eta_0^2}(c_{\gamma'} - c_\gamma) \\ \mathcal{C} &= \frac{6}{\eta_0^3}(c_{\gamma'} - c_\gamma)(c_2 - c_\gamma) \\ \mathcal{D} &= \frac{6}{\eta_0^4}(c_{\gamma'} - c_\gamma)(c_{\gamma'} + 2c_2 - 3c_\gamma) \end{aligned} \tag{4}$$

This choice of the homogeneous free energy density leads to an horizontal common tangent between c_γ and $c_{\gamma'}$.

For Peer Review Only

2.1.2. The Ginzburg-Landau free energy

The non equilibrium "chemical" free energy of the stress free crystal may be approximated by a standard Ginzburg-Landau functional

$$F_{GL} = \int_V \left[f_{homo}(c, \{\eta_i\}) + \frac{\lambda}{2} |\nabla c|^2 + \frac{\beta}{2} \sum_{i=1}^{3} |\nabla \eta_i|^2 \right] dV \tag{5}$$

where the gradient coefficients λ and β are assumed constant. In the above expression, we have used isotropic gradient terms, which implies isotropic interfacial energies. The specific choice of λ and β, and their relation with the relevant interfacial energies of the system are discussed in a forthcoming subsection.

2.2. *The elastic energy*

Elasticity is a key point to understand mesoscale morphological patterns in coherent phase transformations. The elastic energy of a coherent microstructure reads

$$E_{el} = \frac{1}{2} \int_V \underset{\sim}{\boldsymbol{\sigma}} : \underset{\sim}{\boldsymbol{\varepsilon}}^{el} \, dV \tag{6}$$

where $\underset{\sim}{\boldsymbol{\sigma}}$ is the stress tensor and $\underset{\sim}{\boldsymbol{\varepsilon}}^{el}$ the elastic strain tensor. In the case of a coherent phase transformation, the elastic strain is related to the total strain $\underset{\sim}{\boldsymbol{\varepsilon}}$ through

$$\underset{\sim}{\boldsymbol{\varepsilon}}^{el}(\underline{\mathbf{r}}) = \underset{\sim}{\boldsymbol{\varepsilon}}(\underline{\mathbf{r}}) - \underset{\sim}{\boldsymbol{\varepsilon}}^{0}(\underline{\mathbf{r}}) \tag{7}$$

where $\underset{\sim}{\boldsymbol{\varepsilon}}^{0}(\underline{\mathbf{r}})$ is the stress-free strain tensor. Assuming a Vegard's law, the stress-free strain tensor can be expressed using the concentration field

$$\underset{\sim}{\boldsymbol{\varepsilon}}^{0}(\underline{\mathbf{r}}) = \underset{\sim}{\boldsymbol{\varepsilon}}^{T} \Delta c(\underline{\mathbf{r}}) \tag{8}$$

where $\Delta c(\underline{\mathbf{r}}) = c(\underline{\mathbf{r}}) - \bar{c}$, $\bar{c}$ being the average concentration. The transformation strain tensor $\underset{\sim}{\boldsymbol{\varepsilon}}^{T}$ associated to the $\gamma \rightarrow \gamma'$ phase transformation is diagonal ($\varepsilon^{T}_{ij} = \varepsilon^{T} \delta_{ij}$) and its components are given by

$$\varepsilon^{T} = \frac{\delta}{c_{\gamma'} - c_{\gamma}}$$

where δ is the misfit defined as

$$\delta = 2 \, \frac{a_{\gamma'} - a_{\gamma}}{a_{\gamma'} + a_{\gamma}} \tag{9}$$

During diffusive phase transformations, as it is the case in Ni base superalloys, the elastic energy equilibrates much faster than the characteristic diffusion time. When studying the microstructural evolution, it is therefore possible to assume that mechanical equilibrium is always fulfilled. In the case of a microstructural evolution under an applied stress $\underset{\sim}{\boldsymbol{\sigma}}^{a}$, we have

$$\begin{cases} \text{div } \underset{\sim}{\boldsymbol{\sigma}} = 0 \\ \bar{\underset{\sim}{\boldsymbol{\sigma}}} = \underset{\sim}{\boldsymbol{\sigma}}^{a} \end{cases} \tag{10}$$

For Peer Review Only

In the homogeneous modulus case approximation, the mechanical equilibrium can be solved analytically [32]. However, a key point when modeling rafting is the inhomogeneity in elastic properties between the two phases. When the elastic constants of the precipitate and matrix differ, the mechanical equilibrium has to be solved numerically. In the following lines, we detail the fixed point algorithm that we have used. This approach is similar to the ones described in [19, 35, 36].

A periodic media is employed, and the strain tensor is decomposed into a mean value $\bar{\underset{\sim}{\varepsilon}}$ and periodic field $\delta\underset{\sim}{\varepsilon}(\underline{\mathbf{r}})$ (such that $\langle\delta\underset{\sim}{\varepsilon}\rangle = 0$). In the small perturbations framework, the heterogeneous displacement field $\underline{\mathbf{u}}$ is linked to the periodic part of the strain tensor

$$\delta\underset{\sim}{\varepsilon} = \frac{1}{2}\left(\nabla\underline{\mathbf{u}} + (\nabla\underline{\mathbf{u}})^{\mathrm{T}}\right) \tag{11}$$

Hooke's law relates the strain tensor to the stress tensor : $\underset{\sim}{\boldsymbol{\sigma}} = \underset{\sim\sim}{\boldsymbol{\lambda}} : \underset{\sim}{\varepsilon}^{el}$, where $\underset{\sim\sim}{\boldsymbol{\lambda}}$ denotes the local modulus tensor. As explained above, the value of this tensor at point $\underline{\mathbf{r}}$ tensor depends on the structure at point $\underline{\mathbf{r}}$. In a field approach, this is obtained by making the tensor $\underset{\sim\sim}{\boldsymbol{\lambda}}$ dependent on the local value of the fields

$$\underset{\sim\sim}{\boldsymbol{\lambda}}(c(\underline{\mathbf{r}})) = \bar{\underset{\sim\sim}{\boldsymbol{\lambda}}} + \underset{\sim\sim}{\boldsymbol{\lambda}}'\,\Delta c(\underline{\mathbf{r}}) \tag{12}$$

The average modulus tensor $\bar{\underset{\sim\sim}{\boldsymbol{\lambda}}}$ and the heterogeneous modulus tensor $\underset{\sim\sim}{\boldsymbol{\lambda}}'$ are given by

$$\begin{cases} \bar{\underset{\sim\sim}{\boldsymbol{\lambda}}} = \tau_\gamma\ \underset{\sim\sim}{\boldsymbol{\lambda}}^{\gamma} + \tau_{\gamma'}\,\underset{\sim\sim}{\boldsymbol{\lambda}}^{\gamma'} \\ \underset{\sim\sim}{\boldsymbol{\lambda}}' = \dfrac{\underset{\sim\sim}{\boldsymbol{\lambda}}^{\gamma'} - \underset{\sim\sim}{\boldsymbol{\lambda}}^{\gamma}}{c_{\gamma'} - c_\gamma} \end{cases}$$

where $\underset{\sim\sim}{\boldsymbol{\lambda}}^{\gamma}$ and$\underset{\sim\sim}{\boldsymbol{\lambda}}^{\gamma'}$ are the modulus tensors of the γ and γ' equilibrium phases respectively, and where $\tau_\gamma = (c_{\gamma'} - \bar{c})/(c_{\gamma'} - c_\gamma)$ and $\tau_{\gamma'} = 1 - \tau_\gamma$ are the γ and γ' volume fractions expected at incoherent equilibrium.

Using 8 and 12, the following expression can be written for the average stress tensor

$$\bar{\underset{\sim}{\boldsymbol{\sigma}}}(\underline{\mathbf{r}}) = \bar{\underset{\sim\sim}{\boldsymbol{\lambda}}} : (\bar{\underset{\sim}{\varepsilon}} - \langle\underset{\sim}{\varepsilon}^0\rangle) + \underset{\sim\sim}{\boldsymbol{\lambda}}' : \left[\langle\Delta c(\underline{\mathbf{r}})\,\delta\underset{\sim}{\varepsilon}(\underline{\mathbf{r}})\rangle - \langle\Delta c(\underline{\mathbf{r}})\,\underset{\sim}{\varepsilon}^0(\underline{\mathbf{r}})\rangle\right]$$

Using this equation, the boundary condition in 10 can be rewritten as a condition on the average strain

$$\bar{\underset{\sim}{\varepsilon}} = \langle\underset{\sim}{\varepsilon}^0\rangle + \bar{\underset{\sim\sim}{\mathbf{S}}} : \left[\underset{\sim\sim}{\boldsymbol{\lambda}}' : \left(\langle\Delta c(\underline{\mathbf{r}})\,\underset{\sim}{\varepsilon}^0(\underline{\mathbf{r}})\rangle - \langle\Delta c(\underline{\mathbf{r}})\,\delta\underset{\sim}{\varepsilon}(\underline{\mathbf{r}})\rangle\right) + \underset{\sim}{\boldsymbol{\sigma}}^a\right] \tag{13}$$

where $\bar{\underset{\sim\sim}{\mathbf{S}}} = \bar{\underset{\sim\sim}{\boldsymbol{\lambda}}}^{-1}$ is the compliance tensor.

Then, mechanical equilibrium given in 10 is expressed using the heterogeneous

For Peer Review Only

displacement field

$$\bar{\lambda}_{ijkl}\frac{\partial^2}{\partial r_j r_l}u_k = - \frac{\partial}{\partial r_j}\left[\{\bar{\lambda}_{ijkl}+\lambda'_{ijkl}\Delta c(\underline{\mathbf{r}})\}\left[\bar{\varepsilon}_{kl}(\underline{\mathbf{r}})-\varepsilon^0_{kl}(\underline{\mathbf{r}})\right]+\{\lambda'_{ijkl}\Delta c(\underline{\mathbf{r}})\}\frac{\partial}{\partial r_l}\delta\varepsilon_{kl}(\underline{\mathbf{r}})\right] \quad (14)$$

It is convenient to introduce a new symmetric tensor $\underset{\sim}{\mathbf{h}}$ and a new vector $\underline{\mathbf{f}}$ defined as

$$\underset{\sim}{\mathbf{h}}(\underline{\mathbf{r}}) = \{\underset{\approx}{\bar{\lambda}}+\underset{\approx}{\lambda'}\Delta c(\underline{\mathbf{r}})\} : \left[\underset{\sim}{\bar{\varepsilon}}(\underline{\mathbf{r}})-\underset{\sim}{\varepsilon}^0(\underline{\mathbf{r}})\right]+\{\underset{\approx}{\lambda'}\Delta c(\underline{\mathbf{r}})\} : \delta\underset{\sim}{\varepsilon}(\underline{\mathbf{r}}) \quad (15)$$

$$\underline{\mathbf{f}}(\underline{\mathbf{r}}) = \nabla\cdot\underset{\sim}{\mathbf{h}}(\underline{\mathbf{r}}) \quad (16)$$

In Fourier space, the mechanical equilibrium 14 becomes

$$\underline{\mathbf{u}}(\underline{\mathbf{q}}) = \underset{\sim}{\bar{\mathbf{G}}}(\underline{\mathbf{q}})\cdot\underset{\sim}{\mathbf{f}}(\underline{\mathbf{q}}) \quad (17)$$

where the Green operator $\underset{\sim}{\bar{\mathbf{G}}}$ associated with the mean modulus tensor is

$$G^{-1}_{ij}(\underline{\mathbf{q}}) = \bar{\lambda}_{ikjl}\,q_k\,q_l \quad (18)$$

In the homogeneous modulus case (i.e. $\underset{\approx}{\boldsymbol{\lambda}'}=0$) $\underline{\mathbf{f}}(\underline{\mathbf{r}})$ does not depend on the heterogeneous displacement field $\underline{\mathbf{u}}(\underline{\mathbf{r}})$ and (17) is the analytical solution for the heterogeneous displacement field. In the inhomogeneous modulus case, (17) is only a differential equation because $\underline{\mathbf{u}}$ and its derivatives appear on both sides of the equation.

The set of equations 13 and 17 is equivalent to the initial mechanical problem 10. As mentioned above, the average strain tensor $\underset{\sim}{\bar{\varepsilon}}$ and the heterogeneous displacement fields $\underline{\mathbf{u}}$ that are the solution of mechanical equilibrium (13)+(17) are computed numerically using a fixed point algorithm.

Knowing $\underline{\mathbf{u}}^{(n)}(\underline{\mathbf{q}})$ and $\underset{\sim}{\bar{\varepsilon}}^{(n)}$ at the (n)th step, we first compute successively $\delta\underset{\sim}{\varepsilon}(\underline{\mathbf{q}})$ and $\delta\underset{\sim}{\varepsilon}(\underline{\mathbf{r}})$. Using (15), we obtain $\underset{\sim}{\mathbf{h}}(\underline{\mathbf{r}})$. Then going to Fourier space we obtain $\underset{\sim}{\mathbf{h}}(\underline{\mathbf{q}})$ and compute $\underline{\mathbf{f}}(\underline{\mathbf{q}})$ using (16). Finally, the values of $\underline{\mathbf{u}}^{(n+1)}(\underline{\mathbf{q}})$ and $\underset{\sim}{\bar{\varepsilon}}^{(n+1)}$ are deduced from 17 and 13.

Iterations of the fixed point algorithm are repeated until convergence is reached. The convergence test that we use is

$$\max_q\left|\underline{\mathbf{u}}^{(n+1)}(\underline{\mathbf{q}})-\underline{\mathbf{u}}^{(n)}(\underline{\mathbf{q}})\right| < \upsilon\; d\;\epsilon^T$$

$$\sum_{i,j}\left|\bar{\varepsilon}^{(n+1)}_{i,j}-\bar{\varepsilon}^{(n)}_{i,j}\right| < \upsilon\;\epsilon^T$$

where d is the lattice spacing of the numerical grid, and υ is a convergence parameter set to 10^{-5}.

During the first time step of the simulation ($t=0$), $\underline{\mathbf{u}}^{(0)}(\underline{\mathbf{q}})$ and $\underset{\sim}{\bar{\varepsilon}}^{(0)}$ are initialized using the homogeneous case solution. For the other time steps (t>0), the first iteration of the mechanical equilibrium algorithm is initialized from the $t-1$ time step. Ni-base superalloys are known to exhibit small differences in elastic constants between the two phases. Consequently, few iterations are needed for this algorithm

For Peer Review Only

to converge. Typically, 2 iterations are needed to reach convergence for the first time step, and only one iteration is needed afterwards.

2.3. *Numerical implementation*

Kinetic equations of the model are discretized on a regular mesh of grid spacing d and are solved in Fourier space. As usual, equations are first written in a dimensionless form. The dimensionless homogeneous free energy density reads

$$\tilde{f} = \frac{f_{homo}}{\Delta f} \tag{19}$$

and the dimensionless stiffness coefficients

$$\tilde{\lambda} = \frac{\lambda}{\Delta f d^2}, \quad \tilde{\beta} = \frac{\beta}{\Delta f d^2} \tag{20}$$

$\tilde{\lambda}$ and $\tilde{\beta}$ are chosen large enough to ensure smooth interfaces at the scale of the grid spacing. Then, using a one dimensional (stress free) simulation, we compute the numerical interfacial energy $\tilde{\sigma}$. The latter is related to the experimental interfacial energy σ through

$$\sigma = \Delta f \, d \, \tilde{\sigma} \tag{21}$$

Elastic energy densities are written in $C_{44}(\varepsilon^T)^2$ unit and the competition between elastic and chemical energies is controlled by the dimensionless coefficient χ

$$\chi = \frac{C_{44}(\varepsilon^T)^2}{\Delta f} \tag{22}$$

2.4. *Control of the coherent equilibrium concentrations*

The common tangent constructution based on the stress-free homogeneous free energy density f_{homo} gives the concentrations of the coexisting phases at incoherent equilibrium. When considering coherent microstructures, concentrations of the coexisting phases may deviate from the ones of incoherent equilibrium [37, 38]. The deviation is stronger when elastic effects are stronger or when the curvature of the free energy minima of f_{homo} is smaller. Therefore, in our phase field model, the parameter that controls this deviation is the dimensionless coefficient χ defined in 22. Using 21, it is clear that χ increases linearly with the grid spacing d. Consequently, when simulating microstructures with a large grid spacing, the concentration inside the coexisting phases may deviate too much from the incoherent values, leading to unphysical values for the concentrations and the volume fraction at coherent equilibrium.

A way to circumvent this problem is to control the concentrations at coherent equilibrium. This can be done by modifying the homogeneous energy density f_{homo} so that the model leads to prescribed concentrations at coherent equilibrium [26]. To do so, we have followed the procedure proposed in [26] and recalled in the next paragraph.

In the case of homogeneous elasticity, the elastic energy has an analytical ex-

For Peer Review Only

pression with respect to the fields [32]

$$E_{el} = \frac{1}{2}\int_{\underline{\mathbf{q}}}^{*} \frac{d\underline{\mathbf{q}}}{(2\pi)^3}\ B(\underline{\mathbf{q}})\ |c(\underline{\mathbf{q}})|^2 \tag{23}$$

where the star denotes the principal value of the integral,

$$B(\underline{\mathbf{q}}) = \underset{\sim}{\boldsymbol{\sigma}}^0(\underline{\mathbf{q}}) : [\underset{\sim}{\boldsymbol{\varepsilon}}^0(\underline{\mathbf{q}})]^* - \underline{\mathbf{q}} \cdot \underset{\sim}{\boldsymbol{\sigma}}^0(\underline{\mathbf{q}}) \cdot \underset{\sim}{\mathbf{G}}(\underline{\mathbf{q}}) \cdot [\underset{\sim}{\boldsymbol{\sigma}}^0(\underline{\mathbf{q}})]^* \cdot \underline{\mathbf{q}} \tag{24}$$

and $\underset{\sim}{\boldsymbol{\sigma}}^0(\underline{\mathbf{q}}) = \underset{\approx}{\boldsymbol{\lambda}} : \underset{\sim}{\boldsymbol{\varepsilon}}^0(\underline{\mathbf{q}})$. Coherent equilibrium concentrations are obtained when elastic energy is at a minimum, which corresponds to an infinite platelet microstructure parallel to the elastic soft directions, i.e. to the directions which minimize $B(\underline{\mathbf{q}})$. Assuming that the platelets are far enough to neglect their mutual interactions, the corresponding energy writes

$$E_{el}^{min} = \frac{B_{min}}{2}\int_{\underline{\mathbf{q}}}^{*} \frac{d\underline{\mathbf{q}}}{(2\pi)^3}|c(\underline{\mathbf{q}})|^2 = \int_{\underline{\mathbf{r}}} \frac{B_{min}}{2}(c-\bar{c})^2 \tag{25}$$

where B_{min} is the minimum of $B(\underline{\mathbf{q}})$ defined in 24.

To ensure that the coherent equilibrium concentration are given by the common tangent construction based on f_{homo}, it is sufficient to replace f_{homo} by

$$f'_{homo}(c,\{\eta_i\}) = f_{homo}(c,\{\eta_i\}) - \frac{B_{min}}{2}(c-\bar{c})^2 \tag{26}$$

This method is in principle exact in the case of homogeneous elasticity. When elastic constants slightly differ between precipitates and matrix, as it is the case in Ni base superalloys, we have found that this approach is still an efficient way to control concentrations at coherent equilibrium.

2.5. *Numerical inputs*

This section details the physical parameters that are used to calibrate the model.

2.5.1. Homogeneous free energy density

In the numerical solution of the model at 950°C, we have used the equilibrium concentrations c_γ=0.15 and $c_{\gamma'}$=0.23 given in [39]. Moreover we choose c_2=0.18 and for simplicity the value of the equilibrium long-range order parameter η_0 is set to 1.

2.5.2. Elastic energy

The experimental quantities needed to compute the elastic energy are the misfit δ and the elastic constants of the γ and γ' phases. Accurate measurements of these quantities are difficult in a multicomponent alloy, mainly because homogeneous samples of the γ and γ' phases with the required composition are not available.

There are many papers dealing with elastic constants of both phases in Ni-base superalloys, in particular for the γ phase (see [40–42] for example).They show that elastic inhomogeneity is about 10% in these materials. The elastic constants that we have used for the phase field simulations at 950°C are presented in table 1. Elastic constants of the γ matrix are deduced from Ref. [40, 41] and average elastic constants of the AM1 superalloy are obtained from [33, 43]. Then, we have followed

For Peer Review Only

Table 1. Elastic constants of γ and γ' phases used in the simulations at 950°C.

Coefficient [MPa]	C_{11}	C_{12}	C_{44}
γ	197	144	90
γ'	193	131	97
AM1	196	137	95

the homogenization approach proposed in [40] to compute the elastic constants of the γ' phase, assuming a volume fraction of the γ' precpitates equal to 68% [33].

We have used the misfit parameter $\delta = -0.1\%$ for AM1 at 950°C, estimated using in situ X-ray diffraction [44].

2.5.3. Interface energy

Accurate determinations of the γ/γ' interface energy are difficult to reach experimentally. Indeed, interface energies are usually deduced from coarsening experiments using approximate LSW-type models [45]. In addition, very low values are obtained. For exemple, in a binary Ni-Al superalloy, a γ/γ' energy of 4mJ.m^{-2} at 700°C has been recently reported [45]. An alternate approach consists in performing atomic simulations and several attempts have been made to compute the γ/γ' interface energy. However, because the expected energy is low, a very accurate potential is needed to predict a reliable interfacial energy. In addition, a special attention has to be paid to the definition of an interfacial energy between two phases differing in lattice parameters, especially when the energy is to be used in a phase field model [46].

In the present case, we need the value of γ/γ' interface energy in the multicomponent AM1 superalloy at 950°C. Because this value is not known, we have chosen to calibrate this parameter on the critical length ℓ_{3D} which characterize the shape transition from spherical to cuboidal precipitates. This critical length can be readily measured on a micrograph and is found close to 50 nm in AM1 superalloys [47]. Then, an analytical link between the critical length ℓ_{3D} and the interfacial energy can be estimated in the homogeneous elasticity framework [32, 46]. Using the formula given in [46] with the misfit $\delta = -0.1\%$, we obtain $\sigma_{3D} \approx 0.6$mJ.m^{-2}.

However, we have only performed here 2D simulations. Therefore, in our simulations, the shape transition corresponds to a circle to square transition. This transition appears when the size of the γ' domains reach the typical size ℓ_{2D}. As shown in [46], ℓ_{2D} differs from ℓ_{3D}, and using the elastic parameters of the γ phase we have $l^c_{2D}/l^c_{3D} \approx 0.125$. Consequently, to reproduce the 3D cross-over length in our 2D simulations, we have used an interfacial energy σ_{2D}=5mJ.m^{-2} which is about eight times larger than σ_{3D}.

2.5.4. Diffusion coefficients

Using a linearization of 1 near c_γ, the mobility coefficient is related to the interdiffusion coefficient by

$$M = D(c_\gamma)/\Delta f \tag{27}$$

where $D(c_\gamma) = D_0 \exp(-\Delta U/kT)$ is the interdiffusion coefficient. Numerical values for D_0 and ΔU are taken from [48] (D_0=1.45 10^{-4}m^{2}s^{-1}, ΔU=2.8 eV). Note that this value for the interdifffusion coefficient reflects the effective diffusivity in a multicomponent superalloy. Its consistency for the AM1 superalloy need to be established. The relaxation parameter L in 2 is taken equal to Md^2.

For Peer Review Only

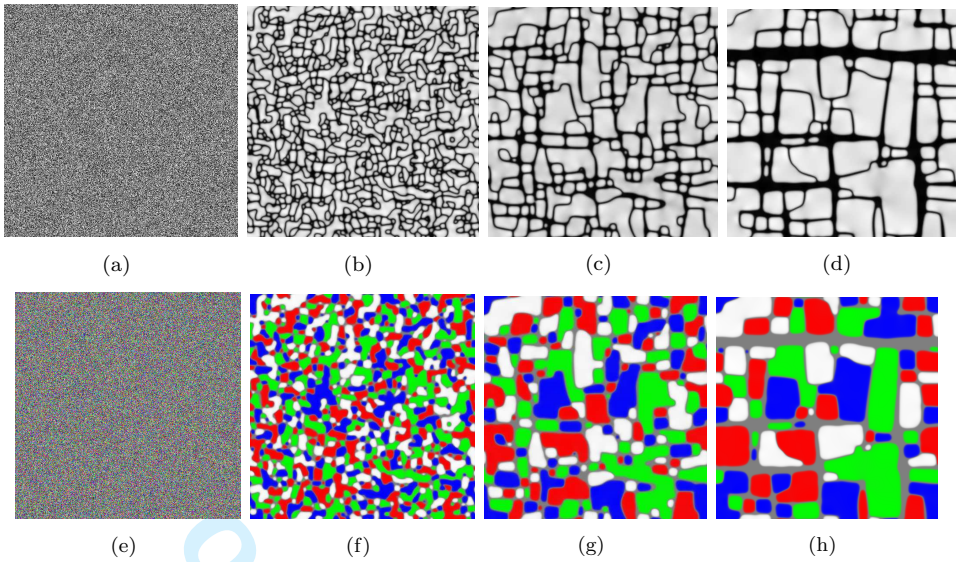


Figure 1. Generation of the cuboidal γ/γ' microstructure, concentration field for (a) t=0, (b) t=1h (c) t=61h and (d) t=180h, order parameters fields for the same times (e) to (h). The simulation box is 10µmx10µm.

2.6. *Generation of the cuboidal microstructure in elasticity*

The aim of the present paper is to study the rafting of the initially cuboidal precipitates observed during a creep loading in a AM1-type superalloy. In this section, we present the results of the phase field model leading to the initial cuboidal microstructure, which will be later used as a starting configuration for the elasto-visco-plastic simulations. Note that the formation of the cuboidal microstructure using phase field models has already been addressed in the litterature, mainly using homogeneous elasticity [49–51], but also in situations where elastic constants of precipitates and matrix strongly differ [36, 52]. In superalloys, the elastic constants of the γ and γ' phases only differ by about 10%, and the influence of elastic inhomogeneity on the microstructural evolution in stress-free condition is expected to be small.

A 2D regular mesh containing 512x512 points has been employed to generate a γ/γ' cuboidal microstructure from a disordered state with stress-free boundary conditions. Since lattice misfit is elastically relaxed in superalloys at 950°C, the generation of the microstructure is performed in the elastic framework. Figure 1 shows the simulated microstructure evolution for an equilibrium volume fraction of 72%. The microstructure development is visualized by shades of gray in accordance with the value of the local composition $c(\underline{\mathbf{r}}, t)$ (figures 1 a-d) and using a color scheme based on the value of local order parameters $\eta_i(\underline{\mathbf{r}}, t)$, where the four translational variants of the γ' phase and the γ matrix appear as different colors (figures 1 e-h). The microstructural evolution starts with the formation of numerous γ' domains (of the four possible translation variants) whose shape is not well defined. During annealing, the mean precipitate size increases, and their shape evolves to reach, after 180 hours, the expected microstructure in Ni-base superalloys, made of cuboidal γ' precipitates aligned along the cubic directions. In this microstructure, γ' are always surrounded by the γ phase, which is consistent with an antiphase boundary energy in the γ' phase which is higher than twice the γ/γ' energy (e.g. [53, 54])

Figure 2 displays a magnified part of the microstructure obtained after 61 hours (figure 1c) containing large cuboidal precipitates and small rather spherical pre-

For Peer Review Only

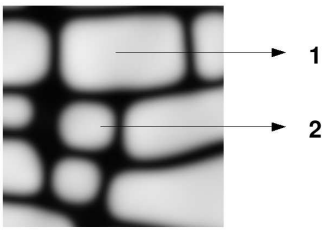


Figure 2. Zoom on the 1(c) picture, size 170nmx170nm.

cipitates. This observation can be used to estimate the critical size ℓ_{2D}, defined in subsection 2.5.3. The precipitate labeled 1, whose size is 82x55nm, is clearly cuboidal whereas the precipitate labeled 2, whose diameter is 35nm, is close to be spherical. Therefore the critical size for the sphere to cube transition is close to 50nm, as it is the case in AM1 superalloys. This validates our choice of the value of the interfacial energy.

Note that the microstructure presented in figure 1d displays a rather large particle size distribution when compared to the microstructure observed in AM1 superalloys (see e.g. [44, 47]). As shown in [36, 52], a narrow size distribution of precipitates is obtained in phase field simulations (with negative anisotropy) when the elastic inhomogeneity is very strong. However, according to the microstructure presented in [36, 52], elastic constants of the precipitate phase should be about twice bigger than the ones of the matrix to obtain a microstructure similar to the one observed in the AM1 superalloy. Such a strong elastic inhomogeneity is in disagreement with all experimental determination of elastic constants in superalloys ([40, 41]). Further investigations are underway to clarify this point.

3. Phenomenological Viscoplasticity

In this section, we present the framework of phenomenological elasto-viscoplasticity which will be later coupled to the phase field equations. A continuum mechanics approach is used within the small perturbations approximation, assuming isothermal conditions. In this context, the total strain tensor $\underset{\sim}{\varepsilon}$ can be decomposed into an elastic and a plastic part

$$\underset{\sim}{\varepsilon}(\underline{\mathbf{r}}) = \underset{\sim}{\varepsilon}^{el}(\underline{\mathbf{r}}) + \underset{\sim}{\varepsilon}^{p}(\underline{\mathbf{r}}) \tag{28}$$

A great number of models have been developed to identify, in a phenomenological way, the plastic strain tensor from macroscopic experiments. Generally speaking, the mechanical approach to plasticity assume the existence of thermodynamic state variables which describe the material. Consequently, a free energy density per unit volume f_{vp} which links state and internal variables can be defined. Denoting M_k a state variable and m_k its dual internal variable, the following relations can be written

$$m_k = \frac{\partial f_{vp}}{\partial M_k} \tag{29}$$

$$\tag{30}$$

For a complete review we refer to [55].

Single crystals of superalloys have an anisotropic macroscopic behavior. At high temperature, they also exhibit a loading rate dependent (visco-plastic) behavior

For Peer Review Only

[56]. The following section describes the model developed for this kind of materials.

3.1. *The crystal plasticity framework*

This model has been proposed by Cailletaud et al. [56, 57]. Plastic deformation in single crystals occurs due to slip on crystallographic systems. In the small perturbations framework, the plastic deformation tensor reads as the sum of the shear strain γ^s over all slip systems s

$$\underset{\sim}{\varepsilon}^p = \sum_s \gamma^s \underset{\sim}{\mathbf{m}}^s \tag{31}$$

where $\underset{\sim}{\mathbf{m}}^s = \frac{1}{2}\left(\underline{\mathbf{l}}^s \otimes \underline{\mathbf{n}}^s + \underline{\mathbf{n}}^s \otimes \underline{\mathbf{l}}^s\right)$ is the orientation tensor for the system s. $\underline{\mathbf{n}}^s$ denotes the normal of the slip plane and $\underline{\mathbf{l}}^s$ the slip direction. The plastic shear γ^s on each slip system is determined from a constitutive model based on the Schmid criterion which states that plastic slip occurs when the resolved shear stress on a slip system reaches a critical value r_0. The resolved shear stress for the s slip system reads

$$\tau^s = \underset{\sim}{\boldsymbol{\sigma}} : \underset{\sim}{\mathbf{m}}^s \tag{32}$$

A Norton's type flow rule is used for the shear strain rate on each system

$$\dot{\gamma^s} = \left\langle \frac{|\tau^s - x^s| - r^s - {r_0}^s}{k} \right\rangle^n sign\left(\tau^s - x^s\right) \tag{33}$$

In 33 $\langle a \rangle$ is the positive part of a. n and k are the Norton's law coefficients and r_0^s the initial thereshold. r^s and x^s refer respectively to isotropic and kinematic hardening on the s slip system. Isotropic hardening is employed to described hardening generated by the dislocation forests. Kinematic hardening traduces a translation of the elastic domain in stress space. For the AM1 superalloy, isotropic hardening is negligible [58]. A non-linear evolution law is adopted for the kinematic hardening

$$x^s = c^s \alpha^s \quad \text{with} \quad \dot{\alpha}^s = \dot{\gamma^s} - d^s |\dot{\gamma^s}| \alpha^s \tag{34}$$

In 34, α^s denotes the kinematic hardening state variable, and c^s are d^s phenomenological coefficients.

These considerations leads to the following hardening free energy

$$f_{vp} = \frac{1}{2} \sum_s c^s (\alpha^s)^2 \tag{35}$$

Single crystal superalloys deform via slip in the octahedral planes due to their crystallography. Each of the 12 octahedral systems is described by its slip direction $\langle 011 \rangle$ and the slip plane normal $\{111\}$. However, for $\langle 111 \rangle$ oriented loading, the macroscopic slip occurs via cubic systems. Authors [59] have shown that this macroscopic cubic slip is due, at microscale, to octahedral slip in zig-zag due to confinement of dislocations in matrix channels. But at macroscale, everything happens as if we can write a Schmid law for cubic systems. This is the reason why cubic slip systems are usually added to the octahedral systems when modeling the macroscopic plastic behavior of superalloys [56, 58]. The incorporation of cubic systems in a macroscopic model is important to reproduce the anisotropy of the

For Peer Review Only

plastic behavior with respect to the loading axis. In our simulations, we have introduced both octahedral and cubic slip systems, even if cubic slip systems are not important when considering a $\langle 001 \rangle$ loading axis.

3.2. *Fitting the visco-plasticity parameters*

This subsection details the method that we have used to select the visco-plastic parameters for both phases.

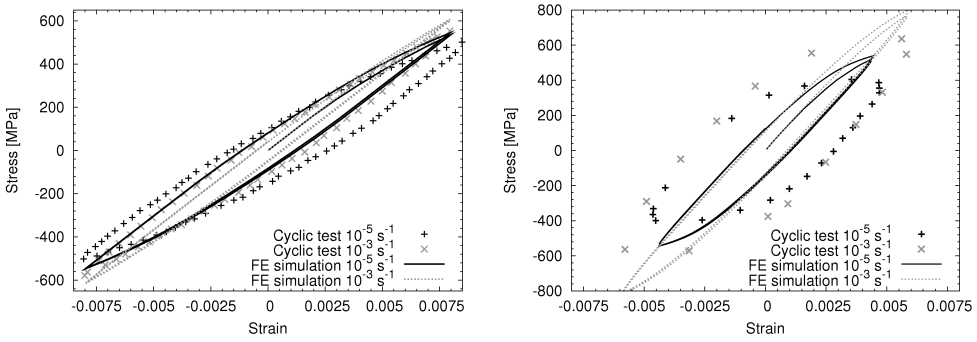
Two problems are faced when identifying visco-plastic parameters for γ and γ' phases. First, their mechanical behavior in the superalloy is not clearly known. In [33, 60, 61], idealized γ bulk materials has been processed and mechanically tested. However, these experiments are not relevant to identify the matrix behavior in the superalloy. The reason is that the dislocations behavior in the narrow channels of the γ matrix differs from the plastic behavior of the bulk γ phase. More generally, dramatic length scale effects are encountered in the superalloys mechanical behavior [62]. This is a well known metallurgical fact that the wider the γ channels, the softer the macroscopic behavior of the superalloy. Because of the lack of experimental data on the behavior of γ and γ' phases at mesoscale in the superalloy, visco-plastic parameters for both phases have to be identified from the effective macroscopic behavior of the superalloy. Nevertheless, an asumption can be made to reduce the number of parameters to be identified. It is known from experimental data on the critical resolved shear stress of both phases [63, 64] and TEM observations that the γ phase accomodates the main part of the plastic deformation (e.g. [65]). This is true for primary and secondary creep stage at high temperature [66, 67] and monotonic or cyclic loadings at low stress levels and high temperature [68]. In conclusion, in the present model the γ' phase is considered elastic.

The second difficulty is related to the microstructural evolution observed particularly during creep experiments. Indeed, it is possible to deduce the mechanical behavior of the channels of γ phase using macroscopic experiments on the AM1 superalloy, only if the microstructure of the alloy does not evolve during the experiment. Consequently, we have chosen to identify material parameters on monotonic and cyclic tests performed on the AM1 superalloy at different orientations and strain rates [58] for which no microstructural evolution is reported.

The strategy developed here to identify the complete set of material parameters of the γ phase is based on an backwards procedure. We search iteratively a set of parameters that reproduces the effective macroscopic behavior of AM1. The finite elements method is used here to simulate the behavior of the γ/γ' material. The microstructure is supposed to be periodic and homogenization methods are employed to calculate the macroscopic behavior of the superalloy [69].

Octahedral sets of parameters are identified on $\langle 001 \rangle$ monotonic and cyclic tests assuming that cubic systems do not activate to much. The cubic ones are identified on $\langle 111 \rangle$ tests. Figure 3 presents examples of simulated behavior for AM1 compared to experiments for two different values of the strain rate ($10^{-5}\,\mathrm{s}^{-1}$ and $10^{-3}\,\mathrm{s}^{-1}$). For the $\langle 001 \rangle$ orientation, and for an applied strain amplitude $\Delta\varepsilon = 1.6\%$, simulations are in agreement with experiments for both values of the strain rate whereas for the $\langle 111 \rangle$ oriented tests, the agreement is not as good. For both orientations, the simulated AM1 behavior is too hard in comparison with experiments. Similar results are obtained when simulating superalloys behavior at the phases-scale with elastic precipitates [33]. In [33], it is shown that the accordance between simulations and experiments is significantly improved when accounting for the shearing of precipitates. However, considering the aim of the present model, which is the simulation of creep loadings (i.e. with no significant γ' shearing), the proposed

For Peer Review Only



(a) (b)

Figure 3. Comparison between experiments[58] and finite elements simulations during cyclic tests with strain rates equal to $10^{-5}\,s^{-1}$ and $10^{-3}\,s^{-1}$: (a) $\langle 001\rangle$ orientation ; (b) $\langle 111\rangle$ orientation.

Table 2. γ phase visco-plastic parameters (evp1) identified from macroscopic experiments on AM1 at 950°C. The width of the γ channels is approximately 50nm.

Coefficient	r_0^s [MPa]	n	k [MPa.s$^{1/n}$]	c^s [MPa]	d^s
Octa. systems	35	5	750	2.10^5	2500
Cubic systems	20	5	200	5.10^5	1000

parameters identification is adapted. Finally, table 2 gives the visco-plastic parameters identified for the γ phase. Due to length scale effects mentionned previously, this set of parameters is only relevant for matrix channels width of approximatively 50nm reported for the AM1 superalloy in the cuboidal microstructure [47]. This set of parameters will be referred to as the evp1 set of parameters in the following.

3.3. *A second set of visco-plastic parameters for the γ phase*

A consequence of the two difficulties faced during parameters identification detailled in the previous paragraph (length scale effects and microstructural evolution) is that the γ phase mechanical behavior evolve during creep owing that matrix channel width is reported to increase. The induced softening of the superalloys can be evaluated thanks to the Orowan equation which states that the effective critical resolved shear stress (crss) is proportional to the inverse of the channel width [70]. Based on experiments from [47, 71], the initial channel width of 50nm increases to reach 150nm in the secondary creep regime. From Orowan equation, we can deduce that the crss decreases by a factor of three during this microstructural evolution.

This softening of the γ channels can not be directly introduced in the present modeling because no length scale appear in the visco-plastic equations. In order to account for the softening of matrix behavior during creep, a second set of visco-plastic parameters, hereafter labeled evp2, corresponding to the γ phase in the rafted situation is proposed in table 3. The kinematic hardening parameter c^s and the initial threshold r_0^s for octahedral slip systems have been divided by a factor three without modification of the viscosity parameters in order to reproduce the estimated decrease in the flow stress during rafting. The comparison between the simulated γ mechanical behavior in the cuboidal and rafted situations are presented in figure 4 for the strain rates $10^{-5}\,s^{-1}$ and $10^{-3}\,s^{-1}$.

The two visco-plastic parameters sets proposed here can be seen as two limit cases when simulating creep. The evp1 set is well adapted to the very beginning of creep when the microstructure has not evolve too much from the cube situation.

For Peer Review Only

Table 3. Second set of visco-plastic parameters (evp2) identified for the γ phase in the rafted microstructure at 950°C. The width of the γ channels is approximately 150nm.

Coefficient	r_0^s (MPa)	n	k (MPa.s$^{1/n}$)	c^s (MPa)	d^s
Octa. systems	12	5	750	7.10^4	2500

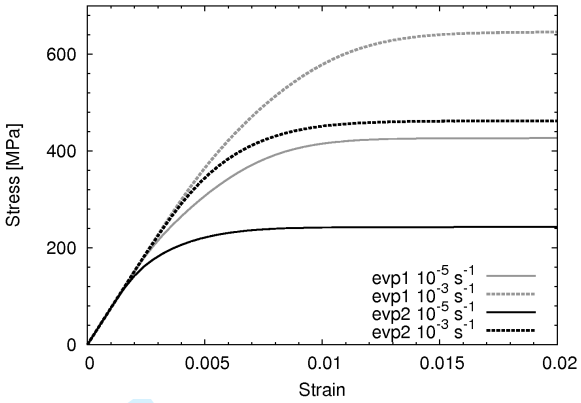


Figure 4. Mechanical behavior of the γ phase for the material parameters set evp1 and evp2. Stress-strain curves are presented for the strain rates $10^{-5}\,s^{-1}$ and $10^{-3}\,s^{-1}$.

The evp2 set represents the matrix behavior once the stable rafted microstructure is reached.

4. Coupling between the phase field model and visco-plasticity

In this part we discuss the construction of a phase field model which takes into account plastic activity. This is realized by coupling the elastic phase field model detailed in section 2 to the visco-plastic model presented in section 3. In this new model, the description of the microstructure is given by four types of fields : the concentration field $c(\underline{\mathbf{r}})$, the order parameters fields $\eta_i(\underline{\mathbf{r}})$, the total strain $\underset{\sim}{\varepsilon}(\underline{\mathbf{r}})$ and the plastic state variables $\alpha^s(\underline{\mathbf{r}})$. The total free energy of the system now reads

$$F = F_{GL} + E_{el} + F_{vp} \tag{36}$$

The dependence of each part of the free energy is to be detailed in order to derive the driving forces. The functional $F_{GL}(c, \{\eta_i\})$ is still given by 5. The elastic energy is now dependant on $c(\underline{\mathbf{r}})$, $\underset{\sim}{\varepsilon}(\underline{\mathbf{r}})$ and on state variables $\alpha^s(\underline{\mathbf{r}})$ through the introduction of the plastic strain tensor $\underset{\sim}{\varepsilon}^p(\underline{\mathbf{r}})$ defined by (28)

$$E_{el}(c, \{\alpha^s\}, \underset{\sim}{\varepsilon}) = \frac{1}{2}\int_V \underset{\approx}{\boldsymbol{\lambda}} : (\underset{\sim}{\varepsilon} - \underset{\sim}{\varepsilon}^0 - \underset{\sim}{\varepsilon}^p) : (\underset{\sim}{\varepsilon} - \underset{\sim}{\varepsilon}^0 - \underset{\sim}{\varepsilon}^p) dV \tag{37}$$

The hardening free energy $F_{vp}(c, \{\alpha^s\})$ is the integral over the sample of the hardening free-energy density 35. $F_{vp}(c, \{\alpha^s\})$ depends on the hardening state variables, but also on the concentration field because the parameters of the visco-plastic model will be made concentration dependent to account for the difference in plastic behavior between the γ and γ' phases.

An important point is that the relaxation of the elastic degrees of freedom is much faster thant the characteristic evolution time of the fields $c(\underline{\mathbf{r}})$ and $\eta(\underline{\mathbf{r}})$ (whose evolution is limited by the diffusion equation 1) but also much faster than the

For Peer Review Only

characteristic evolution time of plasticity (which is limited by viscosity). Therefore, in our kinetic model, it is relevant to assume that elastic equilibrium is always fulfilled.

4.1. *Visco-plasticity parameters in phase field*

The definition of the visco-plastic parameters identified in section 3.2 for pure γ and γ' phases has to be extended to an inhomogeneous situation. In that case, the local value of the visco-plastic parameters at point $\underline{\mathbf{r}}$ should depend on the structure present at that point. In a phase field approach, this is realized by making the the visco-plastic parameter dependent on the local concentration. Therefore, an interpolation scheme similar to the one used for elastic constants is employed for visco-plastic parameters. However, a tanh interpolation has to be employed instead of a linear dependence on the concentration field to avoid numerical divergence, the tanh function being bounded. Denoting X one of the visco-plastic parameter, its dependence on the concentration reads

$$X(\underline{\mathbf{r}}) = \bar{X} + X' \tanh\left(\theta \frac{c(\underline{\mathbf{r}}) - \bar{c}}{c_{\gamma'} - c_{\gamma}}\right) \tag{38}$$

with

$$\begin{cases} \bar{X} = \dfrac{X_{\gamma} + X_{\gamma'}}{2} \\ X' = \dfrac{X_{\gamma} - X_{\gamma'}}{2} \end{cases} \tag{39}$$

θ controls the evolution of the parameter X through the γ/γ' interface. The value θ=-5 has been chosen to ensure $X(c_{\gamma}) = X_{\gamma}$ and $X(c_{\gamma'}) = X_{\gamma'}$ with a precision of 2%.

One can note that a different approach could be adopted for the treatment of plastic activity inhomogeneity. The mechanical state variables themselves could be homogenized in the interface instead of material parameters [29]. Lets recall that the width of the interface is much larger in phase field simulations larger its physical width. Consequently the plastic deformation in the phase field interface has no clear physical meaning. It is why we think that none of these methods is more justified than the other.

As explained above, we consider a visco-plastic behavior for the γ phase but only an elastic behavior for the γ' phase. Within the elasto-visco-plastic framework, a simple way to ensure an elastic behavior for the γ' phase is to set the initial threshold $r_{0\gamma'}$ to a very high value for all slip systems. Taking $r_{0\gamma'}$=1000MPa ensures that γ' will remain elastic for low stress level creep simulations. The other visco-plastic parameters (n, k, c^s, d^s) of the γ' phase are chosen equal to the ones of the γ phase, and will therefore be homogeneous. Using this choice, the only parameters that has to be interpolated using the scheme 38 are the threshold $r_0^s(\underline{\mathbf{r}})$ for octahedral and cubic slip systems.

4.2. *Elastic and visco-plastic driving forces*

In the new model, the temporal evolution of the concentration field $c(\underline{\mathbf{r}})$ and of the order parameter fields $\eta_i(\underline{\mathbf{r}})$ are still given by the usual kinetic equations 1 and 2, but the total free energy is now given by 36.

For Peer Review Only

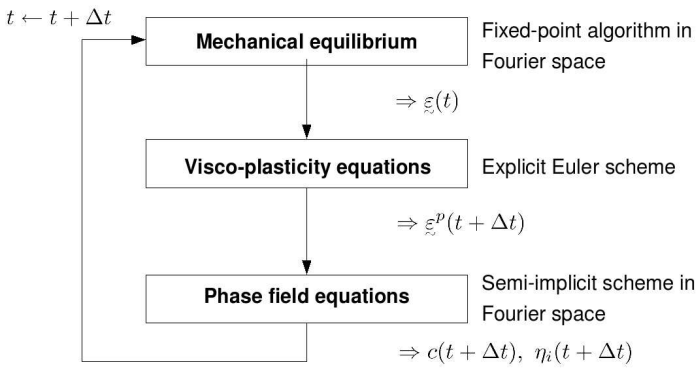


Figure 5. Numerical procedure employed for the resolution of the elasto-visco-plastic phase field model.

The expression of the driving force for the evolution of the order parameter fields $\frac{\delta F}{\delta \eta_i}$ originates only from chemical free energy F_{GL}. On the contrary, the driving force for the evolution of the concentration field $\frac{\delta F}{\delta c}$ has three contributions: the usual chemical driving force $\frac{\delta F_{GL}}{\delta c}$, an elastic driving force and an hardening driving force.

The elastic driving force is obtained by deriving the elastic energy 37 with respect to the concentration field, assuming mechanical equilibrium

$$\frac{\delta E_{el}}{\delta c} = \frac{1}{2}\underset{\approx}{\boldsymbol{\lambda}}' : \underset{\sim}{\varepsilon}^{el} : \underset{\sim}{\varepsilon}^{el} - \left[\underset{\approx}{\bar{\boldsymbol{\lambda}}} + \underset{\approx}{\boldsymbol{\lambda}}'\Delta c\right] : \underset{\sim}{\varepsilon}^{T} : \underset{\sim}{\varepsilon}^{el} \tag{40}$$

with $\underset{\sim}{\varepsilon}^{el} = \bar{\underset{\sim}{\varepsilon}} + \delta\underset{\sim}{\varepsilon} - \underset{\sim}{\varepsilon}^{T}\Delta c - \underset{\sim}{\varepsilon}^{p}$.

The hardening drive force on the concentration field is $\frac{\delta F_{vp}}{\delta c}$. F_{vp} depends in principle on the concentration field. However, with the specific choice of materials parameters presented in the previous subsection, c^s is equal in the γ and γ' phases, and therefore F_{vp} becomes independent of the concentration field. As a conclusion, the hardening driving force on the concentration vanishes.

Note that in this model, the coupling between plastic activity and microstructure arises only through the elastic driving force.

4.3. *Numerical resolution of the coupled model*

The procedure used for the numerical integration of the new model is summarized in 5.

At each time step, we first solve the mechanical equilibrium, assuming that the stress free strain $\underset{\sim}{\varepsilon}^0(\underline{\mathbf{r}})$ and the plastic strain $\underset{\sim}{\varepsilon}^p(\underline{\mathbf{r}})$ are fixed quantities. This is realized using the fixed point algorithm detailed in section 2.2, but where the stress free strain tensor $\underset{\sim}{\varepsilon}^0(\underline{\mathbf{r}})$ appearing in 13 and 15 is replaced by $\underset{\sim}{\varepsilon}^0(\underline{\mathbf{r}}) + \underset{\sim}{\varepsilon}^p(\underline{\mathbf{r}})$. At the end of the mechanical equilibrium step, we end up with the updated value of the total strain tensor $\underset{\sim}{\varepsilon}(\underline{\mathbf{r}})$ and of the stress tensor $\underset{\sim}{\boldsymbol{\sigma}}(\underline{\mathbf{r}})$.

The second step is of the procedure is to solve the visco-plastic kinetic equations. To do so, we compute the resolved shear stress on each slip system $\tau^s(\underline{\mathbf{r}})$ using the stress tensor $\underset{\sim}{\boldsymbol{\sigma}}(\underline{\mathbf{r}})$. Then, the new values of the state variables $\alpha^s(\underline{\mathbf{r}})$ are computed, with an Euler scheme, using the kinetic equations 33 and 34. The new value of the plastic strain $\underset{\sim}{\varepsilon}^p(\underline{\mathbf{r}})$ is obtained using 28.

Finally, the last step of the procedure is to compute the evolution of the concentration field $c(\underline{\mathbf{q}})$ and of the order parameter fields $\eta_i(\underline{\mathbf{q}})$, with a semi-implicit scheme, using the usual kinetic equations 1 and 2 in Fourier space.

For Peer Review Only

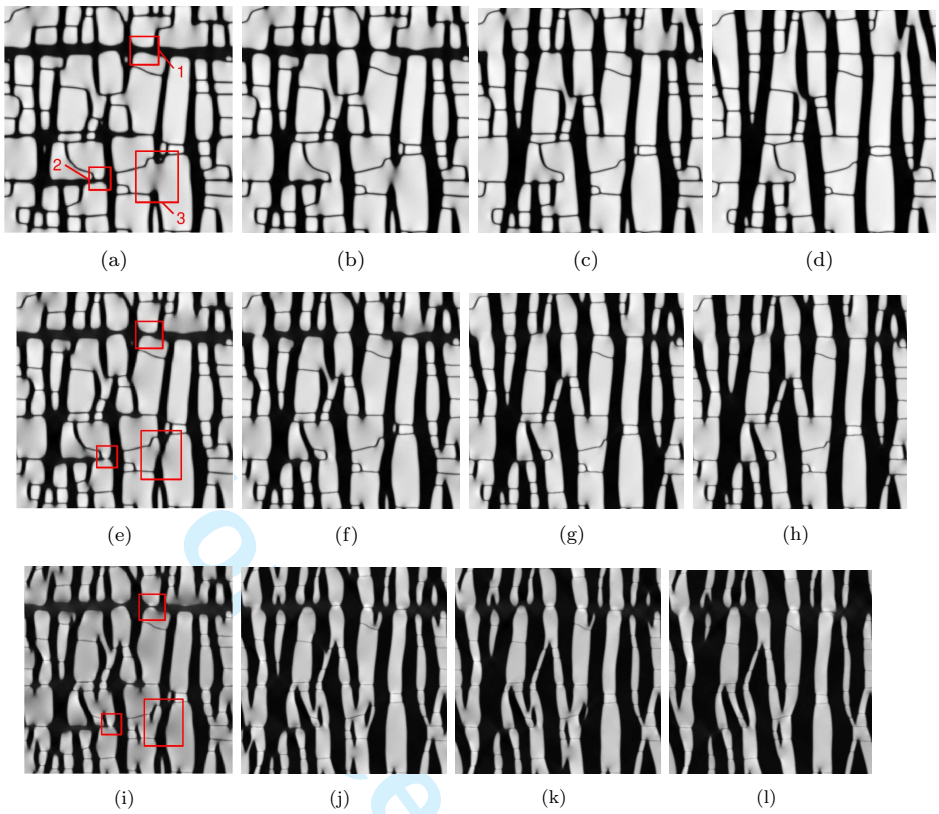


Figure 6. Top: simulated microstructure evolution obtained with the elastic phase field model (a) t=5h (b) t=10h (c) t=20h and (d) t=40h. Middle and bottom: simulation results obtained with the elasto-visco-plastic model at the same times, (e-h) evp1 set of viscoplastic parameters, (i-l) evp2 set.

5. Simulations of rafting

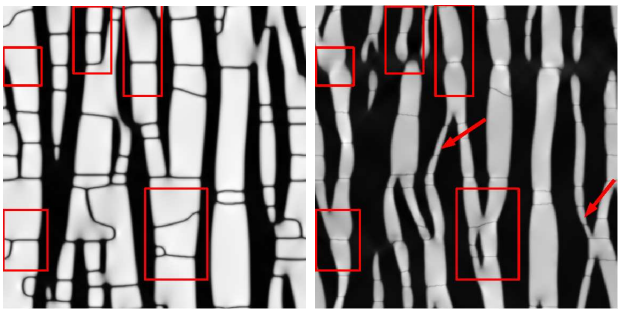
The microstructure evolution during a creep loading of 300MPa at 950°C is simulated with both elastic and elasto-visco-plastic models. Two dimensional simulations are performed using a 512x512 uniform grid. The initial condition is the cuboidal microstructure obtained after 180h annealing in stress free condition (figure 1d).

The microstructure evolutions are presented in figure 6, the tensile axis being horizontal. Top row pictures are the predicted microstructure evolution using the elastic phase field model. The middle and bottom rows are the results of the elasto-visco-plastic phase field model, with evp1 and evp2 sets of parameters respectively. From figure 6, it is clear that rafting of precipitates is observed in the three simulations. The rafts orientation is perpendicular to the tensile axis, in agreement with experimental observations (e.g. [1]).

The comparison of the predictions of the elastic and elasto-visco-plastic models shows that plasticity is active during the creep loading, as it is observed experimentally (e.g. [72]). As detailed below, plastic activity influences both the microstructure evolution and its kinetics.

Because the onset of plasticity is lower with the evp2 set of parameters than with the evp1 set, the plastic activity is less important with the evp1 set than with the evp2 set. This is consistent with the observation that the microstructure evolution obtained with the evp1 set only slightly differs from the predictions of the elastic phase field model, whereas the evolution obtained with the evp2 set is strongly

For Peer Review Only



(a) (b)

Figure 7. Elastic and evp2 rafted microstructures from 6(d) and (k) respectivelly, showing influence of plastic activity on precipitates morphology.

different.

Plastic activity changes the global shape of the rafts. Whereas elastic rafts are quite straight and well-aligned with cubic directions, they are more irregular and with a wavy shape in the simulations using the evp2 set. As shown by the arrow in figure 7, in the presence of a strong plastic activity, the direction of the rafts can substantially deviate from the cubic directions. Inside the rafts, the shape of the γ' precipitates is also clearly modified in the presence of plastic activity, as it is pointed out by the five rectangular regions in figure 7.

Another obvious difference between elastic and visco-plastic simulation results is the evolution of the γ' volume fraction $\tau_{\gamma'}$. In the initial cuboidal microstructure, $\tau_{\gamma'}$ is close to 0.72. During creep, this volume fraction decreases, both with the elastic model ($\tau_{\gamma'} \approx 0.62$) and with the elasto-visco-plastic models ($\tau_{\gamma'} \approx 0.53$ for the evp1 set and 0.33 for the evp2 set). This trend is in agreement with experimental observations in the CMSX-4 superalloy [73]. However, from a quantitative point of view, the decrease of the γ' volume fraction is too large in our elasto-visco-plastic models because the experimental decrease of the volume fraction under a creep loading is only close to 10% [73]. The volume fraction changes originate from the modification of the γ and γ' concentrations between the initial coherent microstructure and the rafted microstructure where coherency stresses are partially relaxed by plasticity. In the phase field model, a smaller evolution of the volume fraction could be obtained by increasing the curvature of the homogeneous free energy density around the minima corresponding to the γ and γ' phases. Further work is underway to improve the model on this point.

The rafted microstructure is made of γ' domains aligned perpendicular to the tensile loading axis. During creep, our simulations predict that, inside a raft, the γ' domains get closer to each other. This effect is more pronounced when plastic activity is taken into account. Note that, in most cases, the neighboring γ' domains are in antiphase relationship and will thus never coalesce to form a single domain. However, in experiments, two γ' domains initially in antiphase relationship may coalesce in the presence of plastic activity [74]. Indeed, when a dislocation of the matrix (whose Burgers vector $\underline{\mathbf{b}}$ is of the type $1/2[110]$) crosses the channel delimited by the two γ' domains, the relative position of the two γ' domains is shifted by $\underline{\mathbf{b}}$. Therefore, the antiphase relationship between the γ' domains changes and may vanish, leading to a possible coalescence of the γ' domains. In a phase field model, this phenomenon could be accounted for by introducing a coupling between the order parameter fields and the plastic activity.

Another consequence of the plastic activity is the speed-up of the morphological changes leading to the rafted structure. This point is illustrated after 5h of creep

For Peer Review Only

by the three caracteristic areas presented in figures 6a-e-i. Area labeled 1 shows that two γ' domains, which are in antiphase relationship and which come close to each other to form a raft, are still quite far away from each other in the elastic simulation after 5h, whereas they are already in contact in the in elasto-visco-plastic simulation with the evp2 set. In the area labeled 2, two γ' domains of the same variant coalesce to form a raft. After 5 hours, the domains are still well separated in the elastic simulation, while they have already coalesced in the evp2 simulation. Finally, rafting proceeds not only by directional coalescence of precipitates, but also by splitting of large precipitates leading to the creation of vertical channel of γ structure. This microstructural evolution can be seen inside the area labeled 3. Comparison of figures 6a-e-i reveals that the splitting of precipitates is also much faster when plastic activity is introduced in the model. As a conclusion, our simulations predict that plastic activity significantly increases the rafting kinetics. Similar trends are shown in [9].

In figure 8, the time evolution of the average plastic strain is plotted and compared to experimental data measured on the AM1 superalloy [47]. The lower creep curve corresponds to the simulation results based on the evp1 set of visco-plastic parameters, which were computed using the initial microstructure. As explained in subsection 3.3, the evp1 set of parameters is expected to well reproduce the plastic activity in the beginning of primary creep, and to underestimate it in the next stages of the microstructure evolution. As shown in figure 8, this prediction is in good agreement with experimental measurements at the very beginning of creep. The upper creep curve in figure 8 is the simulation result obtained with the evp2 set of parameters, where the onset of plasticity was reduced to account for the increase of the γ channel width during the primary creep stage. As expected, this set of parameters overestimates the plastic activity during the first moments of the creep experiment. However the difference in plastic strain between this simulation and experimental data is also a result of the decrease in the γ' volume fraction. This result illustrates difficulties related to material parameters identification for continuous plasticity models and pointed out in section 3.2. The situation is quite complex in the present case where microstructure is evolving and for which it is difficult to decouple plastic strain and plastic strain rate resulting of hardening and viscosity of the widening matrix, morphological evolution of precipitates and decrease in γ' volume fraction. For viscosity, we want to recall that, as explained in section 3.2, viscoplasticity parameters have been identified on monotonic and cyclic tests performed at $10^{-5}\,\mathrm{s}^{-1}$ and $10^{-3}\,\mathrm{s}^{-1}$. During creep, the strain rate is approximatively $5.10^{-5}\,\mathrm{s}^{-1}$ [47] in the secondary stage of creep in the present conditions. This rate allows plasticity recovery mechanisms as modeled in [75]. In the viscoplasticity framework, sinus hyperbolic type flow rules and static recovery potential are commonly used to improve the description of creep [55]. Such recovery mecanisms are not accounted for in the proposed model.

Moreover, after some 25h of creep, the experimental curve shows a strong increase in the plastic strain rate corresponding to the tertiary creep stage which is not observed in simulations. As reported in the literature (e.g. [67]), the onset of tertiary creep is associated with shearing of the precipitates and internal crack initiation from porosity. Theses phenomena are not currently included in the present model. The plastic activity of the γ' phase could be added in the model formulation presented in section 3, but damage mechanics should be employed to account for cracks initiation [67].

A better understanding of the microstructural evolution is obtained by analyzing mechanical fields. The stress component $\sigma_{11}(\underline{\mathbf{r}})$, the total strain component $\varepsilon_{11}(\underline{\mathbf{r}})$, and the plastic strain component $\varepsilon^p_{11}(\underline{\mathbf{r}})$ at t=10h are presented in figures 9, 10

For Peer Review Only

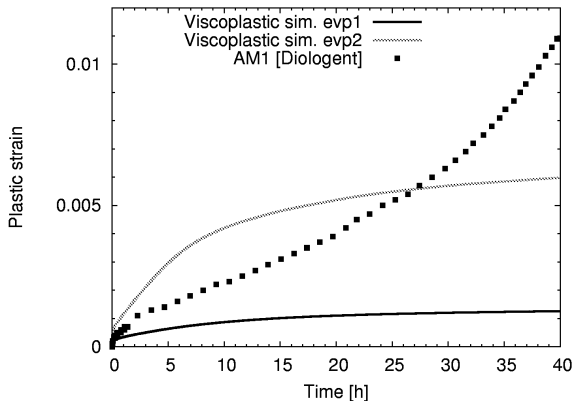


Figure 8. Evolution of the simulated plastic strain with respect to time and comparison with experimental data on AM1 (creep 950°C, 300MPa) [47].

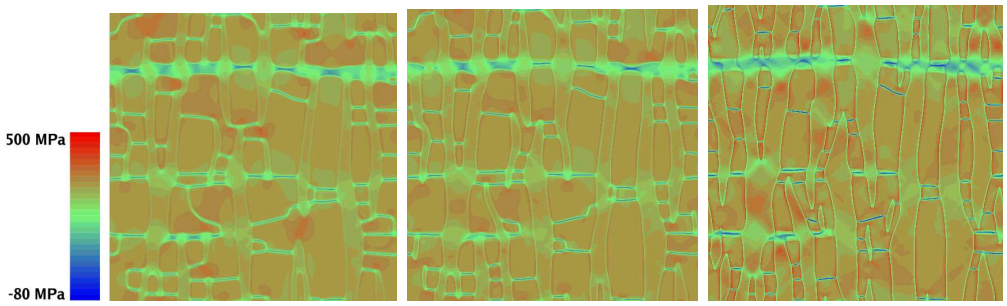
and 11 respectively. These fields show clearly that the mechanical behavior of the vertical and horizontal channels is very different. Plastic activity is mainly present in channel perpundicular to the tensile axis as reported in the literature (e. g. [65]).

In horizontal γ channels, the total strain component $\varepsilon_{11}(\underline{\mathbf{r}})$ is almost equal to that of the neighboring γ' domains, so that the horizontal channels are hardly visible in figure 10. This point is observed in the elastic model but also in the elasto-visco-plastic models. This behavior can be easily understood by analogy with the problem of the thin plate inclusion, the thin horizontal γ channel being the inclusion embedded in a γ' matrix. As shown in [32], the equilibrium state of a thin plate-like inclusion is realized when the total strain is homogeneous in the whole sample and equal to that of the matrix in the absence of inclusion. This result, derived within the elastic framework, explains the mechanical behavior of the horizontal γ channel in the elastic model (figure 10a). Moreover, as it can be seen in figure 11, the plastic strain is negligible in the thin horizontal γ channels. Therefore, the plate-like inclusion analogy used within the elastic framework to explain that $\varepsilon_{11}(\underline{\mathbf{r}})$ has the same value in the horizontal γ channel and in the surrounding γ' domains, remains valid to analyze the horizontal γ channels in the elasto-visco-plastic models.

The vertical γ channels behave quite differently. As shown in figure 10, the strain component $\varepsilon_{11}(\underline{\mathbf{r}})$ is mainly localized inside these channels. This is already true in the elastic model (figure 10a) because the γ' precipitates are stiffer than the matrix. However, the localization is much more pronounced in the elasto-visco-plastic models because of plasticity which has developed in the γ channels. By comparing figures 10 and 11, we conclude that, after 10 hours, the value of the component $\varepsilon_{11}(\underline{\mathbf{r}})$ is mainly due to the elastic strain in the evp1 simulation, whereas it is mainly due to plastic strain in the evp2 simulation.

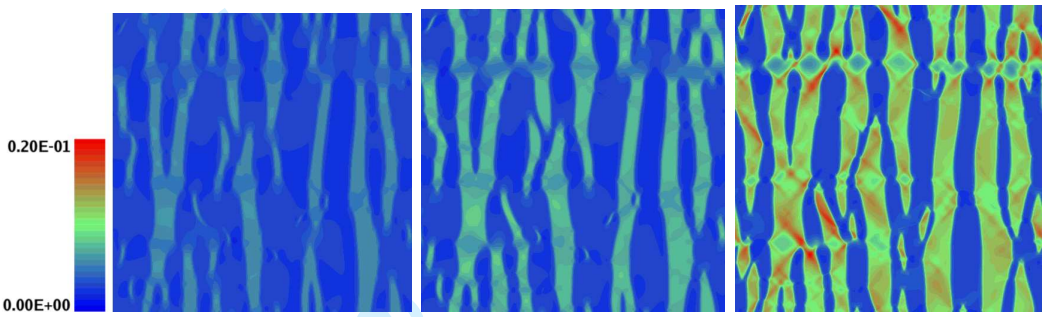
Plastic deformation inside vertical γ channels is not homogeneous. As it can be seen in figure 11b, the values of the plastic strain component $\varepsilon^p_{11}(\underline{\mathbf{r}})$ show strong maxima along directions at 45° from the tensile loading axis. These directions are the directions where Schmid factor is maximal, i.e. where the resolved shear stress (due to the applied tensile loading) is maximal [70]. A consequence of this anisotropy of the plastic activity is to allow the formation of rafts with orientations away from the cubic directions.

For Peer Review Only



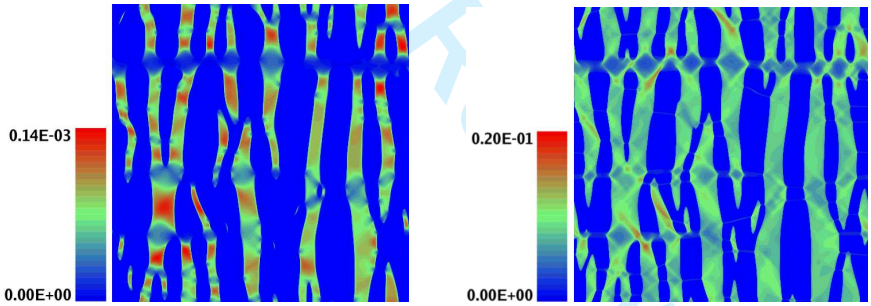
(a) (b) (c)

Figure 9. σ_{11} field at t=10h (a) elastic simulation, (b) evp1 simulation, (c) evp2 simulation.



(a) (b) (c)

Figure 10. ε_{11} field at t=10h (a) elastic simulation, (b) evp1 simulation, (c) evp2 simulation.



(a) (b)

Figure 11. ε^p_{11} field at t=10h (a) evp1 simulation, (b) evp2 simulation.

5.1. *Discussion*

In this paper, we have developed a phase field model coupled to a continuum crystallographic visco-plastic model. This model has been applied to describe the microstructural evolution during a creep loading in a model AM1 superalloy. The results of the model, both concerning the microstruture evolution and the macroscopic behavior are in good agreement with experimental observations.

However, several assumptions have been made in the development of the model. The first one is to assume that a continuum plasticity model is relevant to describe plastic activity at mesoscale. This approach has already been applied for instance in [33, 69, 76]. During creep, this assumption is questionable during the first steps of the microstructural evolution because the γ channels contain only few dislocations, but becomes more realistic during the secondary creep stage when many dislocations evolve and interact with the microstructure.

Other mesoscale models have been developed to describe plastic behavior of superalloys, in which plasticity is described using dislocations [24, 25, 77]. These

For Peer Review Only

approaches have the advantage to introduce the topological defects at the origin of the plastic behavior, and therefore automatically contain several properties such as the link between the width of the channels and the critical resolved shear stress necessary to cross the channels. However, at the present state, these approaches are not able to reproduce in a quantitative way several phenomena which are important during a creep experiment at high temperature. This is especially true for thermally activated phenomena, such as cross-slip and climb of dislocations at γ/γ' interfaces. When using a continuum plasticity model, the consequences of these phenomena are at least partially included in the model, through the adjustment of the viscosity coefficients.

Results presented in the previous section show that plastic length scale effets have a key role on the creep behavior. Indeed, the microstructure evolutions obtained with the evp1 set (channel width $\approx$ 50nm) and evp2 set of parameters (channel width $\approx$ 150nm) strongly differ. Therefore, the softening of the matrix behavior as channel width is increasing has to be taken into account in oder to obtain realistic rafts morphologies and realistic plastic strain rate at macroscopic scale. Because the coupling between the channel width and the softening of the matrix is not taken into account in the present model, we have only simulated two limiting cases, one corresponding to the initial width of the channels (evp1), and the other one to the the channel width observed when the stable rafted microstructure is established. It is of course highly desirable to improve this aspect of the model and to introduce, within a continuous plasticity model, a coupling between the channel width and the plastic behavior of the matrix. This can be done by using a generalized continuum approach, such as a Cosserat continuum [78], or a strain gradient plasticity model (e.g. [79, 80]).

Finally, it is important to note that we have only performed here two dimensional simulations. Our simulations are in fact equivalent to three dimensional simulations, where it is assumed a translational invariance along the [001] cubic axis. Note however that the model can be straightforwardly used for three dimensional simulations. We are planing to perform 3D simulations in the near future because 3D effects may have important consequences when considering microstructural evolution and crystal plasticity.

6. Conclusion

We have developed a phase field model coupled to a continuum crystal plasticity model. This model has been applied to study the microstructural evolution of a model AM1 superalloy during a creep loading. This model takes into account many important physical phenomena, such as the long-range order in the γ' domains, elastic inhomogeneity, plastic activity as well as its anisotropy and viscosity. A special attention has been paid to the determination of the visco-plastic parameters from experiments. Two sets of visco-plastic parameters have been obtained, dedicated to the description of the plastic behavior of the initial microstructure and to the one of the rafted microstructure.

Two dimensional simulations have been performed. At first, a typical cuboidal microstructure has been obtained using an elastic phase field model in stress free conditions. This microstructure was used as an initial state for the simulations under creep loading (300MPa at 950°C). Results of the model, either concerning the microstructural evolution or the macroscopic plastic strain are in agreement with experiments.

The framework introduced in the present work has allowed a comparison on the respective influence of elastic and plastic driving forces on rafting in Ni base su-

For Peer Review Only

peralloys. In the considered conditions, we show that viscoplasticity allows rafts misalignement with cube direction as seen in experiments and increases the rafting kinetics. Moreover, this coupled phase field viscolaplastic model opens new possibilities in the simulation of microstructural evolution under mechanical loading when plasticity can not be negleted. In particular, in the domain of superalloys, a 45° oriented microstructure is observered under a cyclic alternate loading at high temperature [81]. The induced softening of the material during microstructural evolution could be studied within this kind of framework.

Acknowledgements

The authors are grateful to J. L. Chaboche, S. Forest, F. Gallerneau and S. Kruch for fruitful discussions.

References

[1] J.K. Tien and S.M. Copley, Metall. Trans. 2 (1971) p.215–219.
[2] C. Carry and J.L. Strudel, Acta Metall. 26 (1978) p.859–870.
[3] P. Caron and T. Khan, Mater. Sci. Eng. 61 (1983) p.173–184.
[4] R.A. MacKay and L.J. Ebert, Metall. Trans. A 16 (1985) p.1969–1982.
[5] A. Pineau, Acta Metall. 24 (1976) p.559–564.
[6] D.J. Arrell and J.L. Vallès, Scr. Metall. Mater. 30 (1994) p.149–153.
[7] J.Y. Buffière and M. Ignat, Acta Metall. Mater. 43 (1995) p.1791–1797.
[8] N. Ratel, G. Bruno, P. Bastie and T. Mori, Acta Mater. 54 (2006) p.5087–5093.
[9] N. Zhou, C. Shen, M. Mills and Y. Wang, Acta Mater. 56 (2008) p.6156–6173.
[10] M. Véron, *Etude et modélisation de la coalescence orientée dans les superalliages à base de nickel*, Institut National Polytechnique de Grenoble, 1995.
[11] M. Fahrmann, E. Fahrmann, O. Paris, P. Fratzl and T.M. Pollock, *An experimental study of the role of plasticity in the rafting kinetics of a single crystal Ni-base superalloy*, in *Superalloys 1996*, Champion, Pennsyslvania; USA, 1996, pp. 191–200.
[12] N. Matan, D.C. Cox, C.M.F. Rae and R.C. Reed, Acta Mater. 47 (1999) p.2031–2045.
[13] V. Brien, L.P. Kubin and B. Décamps, Phil. Mag. A 81 (2001) p.2285–2301.
[14] M. Véron, Y. Bréchet and F. Louchet, Acta Mater. 44 (1996) p.3633–3641.
[15] L.Q. Chen, W. Y. and A.G. Khachaturyan, Phil. Mag. Lett. 64 (1991) p.241.
[16] Y. Le Bouar, A. Loiseau and A.G. Khachaturyan, Acta mater. 46 (1998) p.2777–2788.
[17] N. Nishimori and A. Onuki, Phys. Rev. B 42 (1990) p.980.
[18] D.Y. Li and L.Q. Chen, Scr. Mater. 37 (1997) p.1271–1277.
[19] M.P. Gururajan and T.A. Abinandanan, Acta Mater. 55 (2007) p.5015–5026.
[20] F. Leonard and R.C. Desai, Phys. Rev. B 58 (1998) p.8277.
[21] S.Y. Hu and L.Q. Chen, Acta Mater. 49 (2001) p.463.
[22] D. Rodney and A. Finel, in *MRS Symp. Proc.*, Vol. 652, 2001, p. Y4.
[23] Y. Wang, Y. Jin, A. Cuitiño and A. Khachaturyan, Acta Mater. 49 (2001) p.1847–1857.
[24] D. Rodney, Y. Le Bouar and A. Finel, Acta Mater. 51 (2003) p.17–30.
[25] N. Zhou, C. Shen, M. Mills and Y. Wang, Acta Mater. 55 (2007) p.5369–5381.
[26] G. Boussinot, *Etude du vieillissement des superalliages à base nickel par la méthode des Champs de Phase*, Université Paris VI, 2007.
[27] A. Gaubert, A. Finel, Y. Le Bouar and G. Boussinot, *Viscoplastic phase field modelling of rafting in Ni-base superalloys*, in *CMDS11*, Paris; France, 2008, pp. 161–166.
[28] R.L.J.M. Ubachs, P.J.G. Schreurs and M.G.D. Geers, Int. J. Solids Struct. 42 (2005) p.2533–2558.
[29] T. Uehara, T. Tsujino and N. Ohno, J. Cryst. Growth 300 (2007) p.530–537.
[30] X.H. Guo, S.Q. Shi, Q.M. Zhang and X.Q. Ma, J. Nucl. Mater. 378 (2008) p.110–119.
[31] A. Royer, A. Jacques, P. Bastie and M. Véron, Mater. Sci. Eng., A 319 (2001) p.800–804.
[32] A.G. Khachaturyan *Theory of structural transformations in solids*, Wiley, 1983.
[33] L. Espie, *Etude expérimentale et modélisation numérique du comportement de monocristaux de superalliages*, Ecole Nationale Supérieure des Mines de Paris, 1996.
[34] Q. Bronchart, Y. Le Bouar and A. Finel, Phys. Rev. Lett. 100 (2008), 015702 p.015702.
[35] H. Moulinec and P. Suquet, Comptes rendus de l'Académie des sciences 318 (1994) p.1417–1423.
[36] S.Y. Hu and L.Q. Chen, Acta Mater. 49 (2001) p.1879–1890.
[37] J.W. Cahn and F. Larché, Acta Metall. 32 (1984) p.1915–1923.
[38] A.J. Ardell, Modelling Simul. Mater. Sci. Eng. 8 (2000) p.277–286.
[39] J.C. Wang, M. Osawa, T. Yokokawa, H. Harada and M. Enomoto, in *Superalloys 2004*, TMS 2004, 2004.
[40] M. Fahrmann, W. Hermann, E. Fahrmann, A. Boegli, T.M. Pollock and H. Sockel, Mater. Sci. Eng., A 260 (1999) p.212–221.
[41] D. Sieborger, H. Knake and U. Glatzel, Mater. Sci. Eng., A 298 (2001) p.26–33.
[42] H. Yasuda, T. Takasugi and M. Koiwa, Acta metall. mater. 40 (1992) p.381–387.

For Peer Review Only

[43] P. Mazot and J. Fouquet, Memoires et Etudes Scientifiques de la Revue de Métallurgie 89 (1992) p.165–170.
[44] A. Royer, P. Bastie and M. Véron, Acta Mater. 46 (1998) p.5357–5368.
[45] A.J. Ardell and V. Ozolins, Nat. Mater. 4 (2005) p.309–316.
[46] G. Boussinot, A. Finel and Y. Le Bouar, Acta Mater. 57 (2009) p.921–931.
[47] F. Diologent, *Comportement en fluage et en traction de superalliages monocristallins à base de Nickel*, Université de Paris 11-Orsay, 2002.
[48] K. Fujiwara, M. Watanabe, Z. Horita, N. Nemoto, K. Noumi and T. Simozaki, in *International Conference on Solid-Solid Transformations*, JIMIC-3, 1999.
[49] Y. Wang, D. Banerjee, C.C. Su and A.G. Khachaturyan, Acta Mater. 46 (1998) p.2983–3001.
[50] J.Z. Zhu, T. Wang, A.J. Ardell, S.H. Zhou, Z.K. Liu and L.Q. Chen, Acta Mater. 52 (2004) p.2837–2845.
[51] T. Wang, G. Sheng, Z.K. Liu and L.Q. Chen, Acta Mater. 56 (2008) p.5544–5551.
[52] J. Zhu, L.Q. Chen and J. Shen, Modelling Simul. Mater. Sci. Eng. 9 (2001) p.499–511.
[53] R. Kikuchi and J.W. Cahn, Acta Mater. 24 (1979) p.1337.
[54] Y. Le Bouar, A. Loiseau and A. Finel, Phys. Rev. B 68 (2003) p.224203.
[55] J. Lemaître and J.L. Chaboche *Mechanics of solid materials*, , 1985.
[56] L. Méric, P. Poubanne and G. Cailletaud, J. Eng. Mater. Technol. 113 (1991) p.162–170.
[57] G. Cailletaud, *Une approche micromécanique phénomènologique du comportement inélastique des métaux*, Ecole Nationale Supérieure des Mines de Paris, 1987.
[58] F. Hanriot, *Comportement du superalliage monocristallin AM1 sous sollicitations cycliques*, Ecole Nationale Supérieure des Mines de Paris, 1993.
[59] D. Bettge and W. Österle, Scr. Mater. 40 (1999) p.389–395.
[60] M. Benyoucef, *Etude par microscopie in-situ des mécanismes de déformation du superalliage MC2*, Université Paul Sabatier de Toulouse, 1994.
[61] R. Glas, M. Jouiad, P. Caron, N. Clement and O.K. Kirchner, Acta Mater. 44 (1996) p.4917–4926.
[62] D.M. Shah and D.N. Duhl, *The Effect of Orientation, Temperature and Gamma Prime Size on the Yield Strength of a Single-Crystal Nickel-Base Superalloy*, in *Superalloys 1984*, Champion, Pennsylvania; USA, 1984, pp. 105–114.
[63] A. Nitz and E. Nembach, Metallurgical and Materials Transactions A 29A (1998) p.799–807.
[64] M. Demura, D. Golberg and T. Hirano, Intermetallics 15 (2007) p.1322–1331.
[65] T.M. Pollock and A.S. Argon, Acta Metall. Mater. 42 (1994) p.1859–1874.
[66] A. Fredholm, *Monocristaux d'alliages base nickel: relation entre composition, microstructure et comportement en fluage à haute température*, Ecole Nationale Supérieure des Mines de Paris, 1987.
[67] D.W. MacLachlan, L.W. Wright, S. Gunturi and D.M. Knowles .
[68] V. Brien and B. Décamps, Mater. Sci. Eng., A 316 (2001) p.18–31.
[69] D. Nouailhas and G. Cailletaud, Scr. Mater. 34 (1996) p.565–571.
[70] J.P. Hirth and J. Lothe *Theory of dislocations*, Wiley, 1982.
[71] Z. Peng, U. Glatzel, T. Link and M. Feller-Kniepmeier, Scr. Mater. 34 (1996) p.221–226.
[72] T.M. Pollock and A.S. Argon, Acta Metall. Mater. 40 (1992) p.1–30.
[73] K. Serin, G. Göbelini and G. Eggeler, Mater. Sci. Eng., A 387-389 (2004) p.133–137.
[74] C. Chen and W. Stobbs, Metall. Mater. Trans., A 35A (2004) p.733–740.
[75] J. Svoboda and P. Lukás, Acta Mater. 45 (1997) p.125–135.
[76] R. Estevez, G. Hoinard and P. Franciosi, Acta Mater. 45 (1997) p.1567–1584.
[77] B. Devincre, L.P. Kubin, C. Lemarchand and R. Madec, Mater. Sci. and Eng., A 309-310 (2001) p.211–219.
[78] S. Forest, F. Barbe and G. Cailletaud, Int. J. Solids Struct. 37 (2000) p.7105–7126.
[79] E.P. Busso, F.T. Meissonier and N.P. O'Dowd, J. Mech. Phys. Solids 48 (2000) p.2333–2361.
[80] D.L. McDowell, Mater. Sci. Eng., R 62 (2008) p.67–123.
[81] H. Mughrabi, S. Kraft and M. Ott, *Specific aspects of isothermal and anisothermal fatigue of the monocrystalline Nickel-base superalloy CMSX6*, in *Superalloys 1996*, Champion, Pennsylvania; USA, 1996, pp. 335–344.

For Peer Review Only